scientific reports

OPEN

One-pot synthesis of novel chitosan-salicylaldehyde polymer composites for ammonia sensing

Ahmed Muhammed Saeed[1✉], Ahmed Gaber Taha[2], Hemat Mohamed Dardeer[2] & Moustafa Fawzy Aly[2✉]

Chitosan (Chs)-salicylaldehyde (Sal) polymer derivatives were formed via the reaction of Chs-Sal with zinc oxide nanoparticles (ZnO NPs) and beta-cyclodextrin (β-CD). These polymers were synthesized through inclusion with β-CD and doping with ZnO NPs to give pseudopolyrotaxane and Chs-Sal/ZnO NPs composite, respectively, for low-temperature detection and sensing of NH_3 vapors as great significance in environmental control and human health. Additionally, the polymer (Chs-Sal/β-CD/ZnO NPs) was prepared via the insertion of generated composite (Chs-Sal/ZnO NPs) through β-cyclodextrin ring. The structural and morphological characterizations of the synthesized derivatives were confirmed by utilizing FTIR, XRD and, SEM, respectively. Also, the optical properties and thermal gravimetric analysis (TGA) of the synthesized polymers were explored. The obtained results confirmed that using β-CD or ZnO NPs for modification of polymer (Chs-Sal) dramatically enhanced thermal stability and optical features of the synthesized polymers. Investigations on the NH_3-sensing properties of Chs-Sal/β-CD/ZnO NPs composite were carried out at concentrations down to 10 ppm and good response and recovery times (650 s and 350 s, respectively) at room temperature (RT) and indicated that modification by β-CD and doping with ZnO NPs effectively improves the NH_3-sensing response of Chs-Sal from 712 to 6192 using Chs-Sal/β-CD/ZnO NPs, respectively, with low LOD and LOQ of 0.12 and 0.4 ppb, respectively.

Polymers have emerged as inevitable in our daily lives because of their many applications in various fields such as medical[1,2], automobile[3], aerospace[4], electronics[5], packaging[6], and food[7]. It is well known that synthetic polymers are harmful to the environment due to their non-degradation[8]. Therefore, researchers tend to replace these synthetic polymers with biopolymers such as cellulose, chitin, chitosan and, poly peptides[9–12]. However, chitosan is superior to the other bio-polymers due to its crystallinity, nitrogen richness, hydrophilicity, and high viscosity ionic conductivity. Chitosan is extracted from the shells of shrimp and other easily crustaceans[13]. Chitosan's amino group has drawn a lot of attention since it creates a corresponding Schiff base (SB)[14–17]. Numerous uses for this imino group exist, such as sorbents, corrosion inhibitors, medicinal agents, sensors[18,19], and important biological reaction intermediates[16,20–23]. Finally, modification of chitosan through chemical, radiation, enzymatic and, physical methods can produce a biopolymer that has more tendencies to interact with other components[24]. Chitosan has also different active groups such as primary and secondary hydroxyl groups in its monomer, so it can be chemically modified by interaction with other components, such as metal ions, and organic compounds[25].

Cyclodextrin (CD) is well-known type of macrocyclic compound obtained by intermolecular connection of D-(+)-glucopyranosyl units[26]. CDs are one of the oligosaccharides class with an important role in the pharmaceutical research and global market, which are formed by starch under the function of amylase enzyme[27,28]. Primarily, it is separated into three products: α-, β-, and γ-CDs, each consisting of 6, 7, and 8 glucose units. β-CD is typically the most utilized due to its moderate molecular void space and inexpensive production cost, making it more appropriate for a variety of applications[29].

Interestingly, ammonia (NH_3) is used in various fields such as food, industrial, cleaning, and chemical manufacturing[30–32]. Moreover, ammonia has also been utilized as a key signal in the detection of conditions including diabetes, renal illness, malignant tumors, and lung cancer since it is a metabolite in human life[33]. Despite its use, NH_3 is a poisonous gas that is detrimental to human health due to its colorlessness and toxicity[34]. A large dose of ammonia affects negatively on the human body and may cause eye discomfort, sore throat, skin

[1]Department of Chemistry, Faculty of Science, Al-Azhar University, Cairo 11884, Egypt. [2]Department of Chemistry, Faculty of Science, South Valley University, Qena 83523, Egypt. ✉email: ahmed_saeed@azhar.edu.eg; mosfaly51@yahoo.com

irritation, and respiratory system irritation[35]. Inorganic compounds (metal-oxides) and organic materials (conducting polymer) have been the subject of studies on NH_3 gas sensors[18,19,36]. The metal-oxides-based gas sensors may have a high sensing response and low detection limit.

ZnO NPs and polymer/ZnO nanocomposites as NH_3 sensors have been reported by different researches[37–41]. The results demonstrated that the polymer/ZnO nanocomposites exhibited higher response towards NH_3 with good response and recovery times in addition to low limit of detection (LOD).

It was reported by our previous work that the chitosan–N-acetylisatin/β-CD/ZnO NPs composite was used in bone tissue engineering and afforded good results in this field. So, we expected these types of polymers to have many applications in various fields[42], especially in toxic gas sensing.

We study the modification of chitosan-salicylaldehyde (Chs-Sal) polymer through inclusion into β-CDs and doping with ZnO nanoparticles (NPs) to give (Chs-Sal/β-CD)pseudopolyrotaxane and Chs-Sal/ZnO NPs composite. Moreover, modify Chs-Sal polymer through insertion into β-CDs and doping with ZnO nanoparticles (NPs) in one pot reaction to afford (Chs-Sal/β-CD/ZnO NPs) pseudopolyrotaxane composite in a cheap, simple and eco-friendly route. The modified polymers exhibit elevated crystallinity, wide optical properties, and thermal stability making them suitable for wide applications such as toxic vapor and gas sensing.

Materials and methods
Materials
Chitosan (deacetylation degree above 85%, CAS. No = 9012-76-4), salicylaldehyde (98.5%, CAS. No = 90-02-8), β-CD (CAS. No = 7585-39-9), ZnO NPs (purity over 97%, > 50 nm), glacial acetic acid, and dimethylformamide (DMF) (≥ 99.8%) were supplied from Sigma-Aldrich, Milwaukee, Wisconsin, USA. All chemicals and solvents used are of analytical grade and are used as received without further purification.

Synthesis of Chs-Sal polymer
A solution of salicylaldehyde (0.40 g in 10 ml MeOH) was prepared at room temperature with stirring for 6 h before the temperature was raised to 100 °C for 1 h, according to Fig. 1a. Chitosan powder (1.0 g) in 50 ml of glacial acetic acid (1% v/v) was then added. The Chs-Sal polymer was obtained as a yellow powder by evaporating the solvent at room temperature.

Synthesis of pseudopolyrotaxane (Chs-Sal/β-CD)
A mixture of Chs-Sal polymer (1.0 g) and β-CD (2.0 g) in DMF (25 ml) was stirred at room temperature for 24 h, Fig. 1b. The obtained precipitate dried at room temperature to afford Chs-Sal/β-CD as a pale-yellow powder.

Synthesis of Chs-Sal/ZnO NPs composite
A mixture of ZnO NPs (0.10 g) and Chs-Sal polymer (1.0 g) in DMF (25 ml) was agitated for 30 h at room temperature. To obtain green crystals of Chs-Sal/ZnO NPs, the hydrogel that had formed was transferred into a Petri plate and allowed to dry at room temperature (Fig. 1c).

Synthesis of Chs-Sal/β-CD/ZnO NPs composite
For six hours, a solution containing 1.0 g of Chs-Sal polymer and 0.10 g of ZnO NPs in 25 ml of DMF was stirred at room temperature. Next, β-CD (2.0 g) was added to DMF (25 ml) and stirred while left at room temperature for 48 h (Fig. 1d). The formed hydrogel was poured into a Petri dish and dried at room temperature to afford Chs-Sal/β-CD/ZnO NPs composite as a pale-yellow crystal.

Characterizations
Fourier-transformation infrared (FTIR)
FTIR spectroscopy was used to examine the structure of the generated derivatives at room temperature utilizing potassium bromide disc (KBr) (using an infrared spectrometer, a Jasco Model 4100 from Japan), specifically in the wavenumber range of 4000 to 400 cm^{-1}.

X-ray diffraction (XRD)
XRD measurements were performed at room temperature using a powder diffractometer (Brucker D8 Advance, Germany) fitted with a Cu K radiation source, yielding values of = 1.5406 and 2 in the range of (5°–80°) for the crystallite size and phase structure of the polymers

Scanning electron microscope (SEM)
A 20 kV accelerated voltage SEM (JEOL SEM model JSM-5500—Japan) was utilized to examine the morphological structures of the formed derivatives.

Thermogravimetric analysis (TGA)
Using a TGA (SDT Q600 V20.9 Build 20-Germany) with a 5 °C/min heating rate up to 400 °C and a 5 ml/min nitrogen gas flow, the thermal stability of the synthesized derivatives was assessed. A data collecting and handling mechanism is built into the thermal analyzer (TA-50WSI).

UV–visible spectroscopy
The optical characteristics of the produced polymers were determined using UV–visible spectroscopy. The UV–visible spectra were obtained by using a UV–visible spectrophotometer (PG Instruments, model T80, UK)
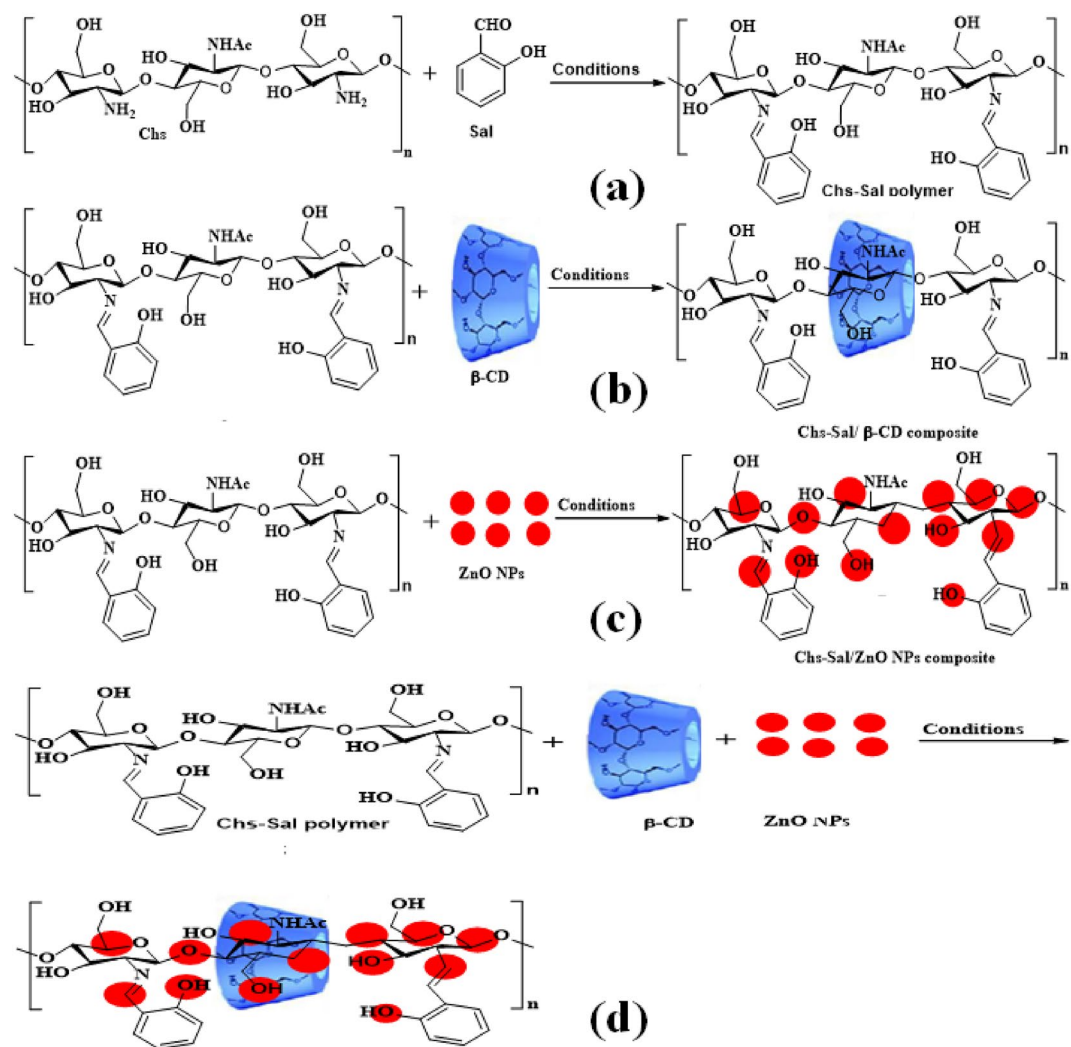
Figure 1. Synthesis of (**a**) Chs-Sal polymer, (**b**) Chs-Sal/β-CD composite, (**c**) of Chs-Sal/ZnO NPs composite, and (**d**) Chs-Sal/β-CD/ZnO NPs composite, respectively.

and quartz cells with a path length of 1 cm with wavelengths ranging from 200 to 800 nm. To modify the baseline, DMF was utilized as a blank.

Gas sensing studies

The sensing properties of the synthesized polymer composites were studied by utilizing a homemade system comprises a 5 L glass chamber and a laptop interfaced digital multimeter for signal acquisition[36,43,44]. The sensor was fabricated by painting the composite paste on interdigital electrode interdigitated electrodes (5 cm × 4 cm × 2 cm) and dried at 45 °C for 24 h.

Different volumes of volatile liquids were injected into the bottle using a syringe to obtain the corresponding concentrations. The relation = Ra/Rg, where Ra and Rg stand for the sensor's resistances in the air and in the presence of the tested gas, respectively, was used to calculate the sensor response. The amount of time it takes to get to 90% of the final equilibrium value is defined as the response and recovery times.

Results and discussion
SEM analysis

Figure 2 shows the SEM images and the surface morphology of chitosan, β-CD, ZnO NPs, and the generated chitosan polymers (Fig. 2a–g). In contrast to the fibrous nature of the chitosan surface, these images demonstrate the apparent differences between them and the surface appearances that were altered upon reaction. As rough, amorphous slides, the Chs-Sal polymer was visible (Fig. 2b). Additionally, the surface morphology of β-CD and pseudopolyrotaxane polymer showed a high difference between them due to the insertion of Chs-Sal polymer into the β-CD (Fig. 2d). Pseudopolyrotaxane polymer showed a scaly and slightly rough structure with a bigger random particle crystal size. SEM images of Chs-Sal/ZnO NPs composite showed smooth slides without pores surface. The pores of Chs-Sal polymer are considered a particle sink to get ZnO NPs inside it to form the
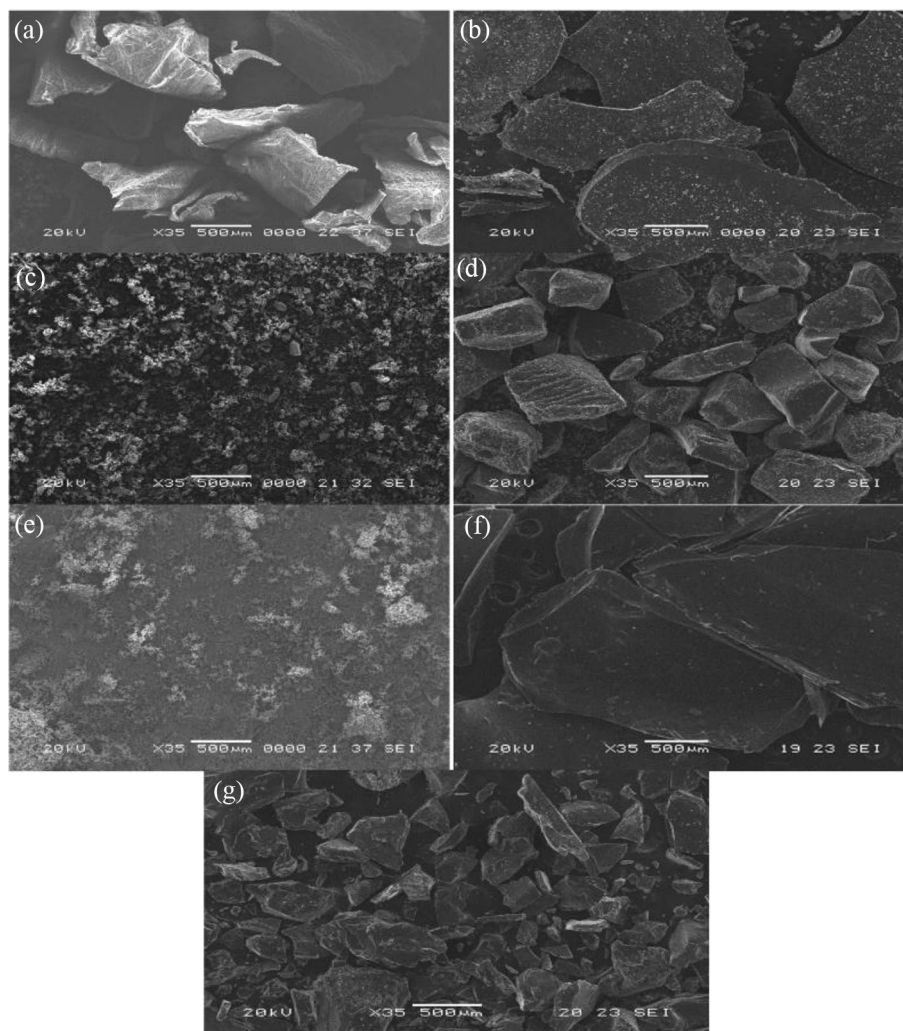
Figure 2. SEM images of (**a**) Chs, (**b**) Chs-Sal, (**c**) β-CD, (**d**) Chs-Sal/β-CD, (**e**) ZnO NPs, (**f**) Chs-Sal/ZnO, and (**g**) Chs-Sal/β-CD/ZnO.

soft surface of the composite (Fig. 2f). The surface morphology of pseudopolyrotaxane polymer was changed in Chs-Sal/β-CD/ZnO NPs composite (Fig. 2g). It has become uneven and aggregated in Chs-Sal/β-CD/ZnO NPs composite.

XRD analysis

The phase structure and crystallite size of chitosan (Chs), Chs-Sal polymer, β-CD, pseudopolyrotaxane polymer, ZnO NPs, Chs-Sal/ZnO NPs, Chs-Sal/β-CD/ZnO NPs composite, were accomplished using XRD analysis (Fig. 3a,b) at 25 °C, in the range of 5° to 80°. The diffraction peaks that are characteristic of Chs were observed at $2\theta = 8.6°$ and 20°, indicating that it is semi-crystalline[45–48]. XRD analysis showed the formation of Schiff base (SB) (Chs-Sal polymer) via the changing of amino group nature. Moreover, the difference in the crystal size and crystallinity of Chs was indicated by disappearance peaks in 16.4°, 33.6°, and the appearance of a slight peak in 13.8°. Additionally, the crystallinity values of Chs and the formed Chs-Sal polymer showed 57.7 and 50.6%, respectively. The crystallinity value of Chs-Sal decreased due to the formation of SB and cleavage of hydrogen bonds[49]. The XRD pattern of pseudopolyrotaxane polymer showed a sharp diffraction angle at 14.2° and the crystallinity value was 48.3% and the crystal size increased compared to Chs-Sal polymer (crystal size values of Chs-Sal and pseudopolyrotaxane polymer were 2.4 and 3.2 nm, respectively). Decreased crystallinity in the case of the pseudopolyrotaxane polymer is due to the Chs-Sal chain being inserted into the electron-rich cavity of the cyclodextrin rings. After addition of ZnO NPs to the Chs-Sal polymer gave a different pattern in XRD analysis. In the blind polymer, a broad peak decreased in intensity and some distinct peaks emerged at 15.9°, 17.9°, and 29.9°. Additionally, the cost of the crystallinity value (46.1%) this difference indicates the formation of hydrogen bonding between Chs-Sal and ZnO NPs. Finally, Chs-Sal/β-CD/ZnO NPs composite XRD result showed broad peaks at 13.3°, 13.7°, 14.2°, 14.6°, 17.6°, 18.2°, higher crystal size 5.78 nm and lower crystallinity value 45%. The Scherrer equation was used to calculate the crystal size of the synthesized polymers[50].
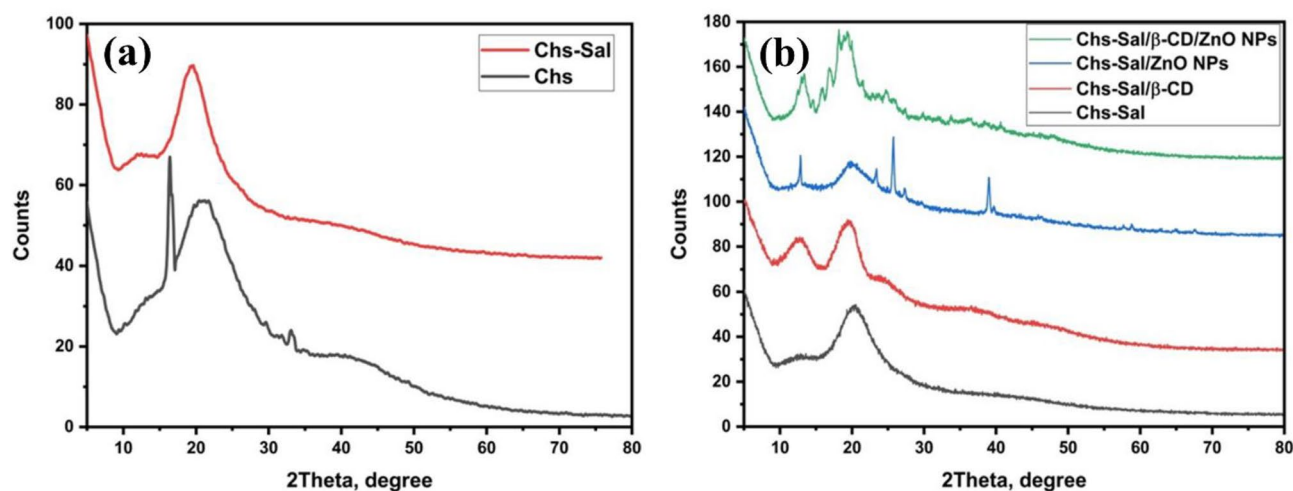
Figure 3. XRD spectra of (**a**) chitosan and chitosan-salicylaldehyde, and (**b**) Chs-Sal, Chs-Sal/β-CD, Chs-Sal/ZnO, and Chs-Sa/β-CD/ZnO.

$$D = K\lambda/\beta\cos\theta$$

where λ is the wavelength of the X-ray; β, the half width of the diffraction peak; θ, diffraction angle; and k, constant. And the crystallinity values were calculated from this equation:

$$\% \text{ Crystallinity} = \left[\left(\text{area under the crystalline peaks} \right) / \left(\text{area under all peaks} \right) \right] \times 100.$$

Fourier-transform infrared spectroscopy (FT-IR)

FT-IR was used to confirm the formation of the components. Figure 4a shows the difference between the Chs and Chs-Sal polymer as a SB. The hydrocarbon bond C–H appeared at 2978 cm^{-1}, and the –OH group characteristic peak in Chs appeared at 3334 cm^{-1}, superimposed over the N–H stretching band. In addition, the peaks of –C=O amide and –NH$_2$ were observed at 1657 cm^{-1} and 1598 cm^{-1}. The spectrum of SB polymer showed C=N band at 1631 cm^{-1} which confirmed the Chs-Sal polymer formation. Additionally, C–C bonds stretching and bending vibrations on the aromatic ring of the aldehyde and the stretching vibration of –C–O of Sal appeared at 1490, 820, and 1250 cm^{-1}, respectively[51–53]. There is no detectable residual of free Sal, as evidenced by the absence of the salicylaldehyde characteristic band in the area 1660–1730 cm^{-1} in the SB spectrum. Table 1 provides a summary of the differences between the absorbance bands of chitosan and Chs-Sal polymer.

It was noticed that the absorption band of the hydroxyl group is slightly high and less intensity than the β-CD sample (Fig. 4a). Also, the ν[OH] symmetric stretching was shifted to a higher frequency and ν[CH-aliphatic] was shifted to a lower frequency compared to those in β-CD. Furthermore, the ν[C–O–C] and ν[CH$_2$-O] bending vibrations were shifted to lower frequencies at 1027 and 1158 cm^{-1}, respectively. These results confirmed the formation of pseudopolyrotaxane polymer through the reaction of Chs-Sal polymer with β-CD. The increase in frequency is due to the Chs-Sal chain being inserted into the electron-rich cavity of the cyclodextrin rings, which accounts for the observation[54]. Conversely, the drop in frequency can be attributed to the formation of hydrogen bonds and Vander Waals forces between the β-CDs and the hydroxyl groups of Chs and Sal molecules, as well as between β-CDs themselves (Fig. 4a). The absorbance bands of pure β-CD, Chs-Sal polymer, and pseudopolyrotaxane polymer are shown to vary in Table 2.

The FT-IR spectrum of the Chs-Sal/ZnO NPs polymer (Fig. 4b), showed a broad absorption band at 3408 cm^{-1} corresponding to the stretching vibrations of hydroxyl (OH) groups. The absorption band at 2945 cm^{-1} is attributed to symmetric stretching of aliphatic C–H groups of Chs in polymer blend[14], which is markedly shifted and decreased in intensity (2930 cm^{-1}) upon doping of ZnO NPs. The absorption band at 1660 cm^{-1} is assigned to free C=O stretching vibration[55]. The absorption bands at 1560 and 1413 cm^{-1} corresponding to the polymer (C=N) group bending[56] and stretching vibration of (CH$_2$–OH), were shifted towards higher wave numbers and decreased in their intensities, because of the interaction between the polymer blend chains and the ZnO NPs[57]. The band at 1073 cm^{-1} which is attributed to C–O–C stretching became less intense and was shifted to lower wavenumber. Table 3 summarizes the variations in absorption bands between Chs-Sal polymer and Chs-Sal polymer doped with ZnO NPs.

These changes (shift and decreased intensity) indicated the strong interaction between these functional groups in the polymer blend and ZnO NPs. The absorption band at 675 cm^{-1} appeared due to the stretching mode of the amide groups attached to ZnO NPs[58,59] (Fig. 4b).

Figure 4c shows the difference between Chs-Sal polymer, Chs-Sal/ZnO NPs composite, Chs-Sal/β-CD, and Chs-Sal/β-CD/ZnO NPs composite. The FT-IR spectrum of the Chs-Sal/β-CD/ZnO NPs composite showed a broad absorption band of OH group at 3375 cm^{-1} with increasing intensity compared to the last polymers.
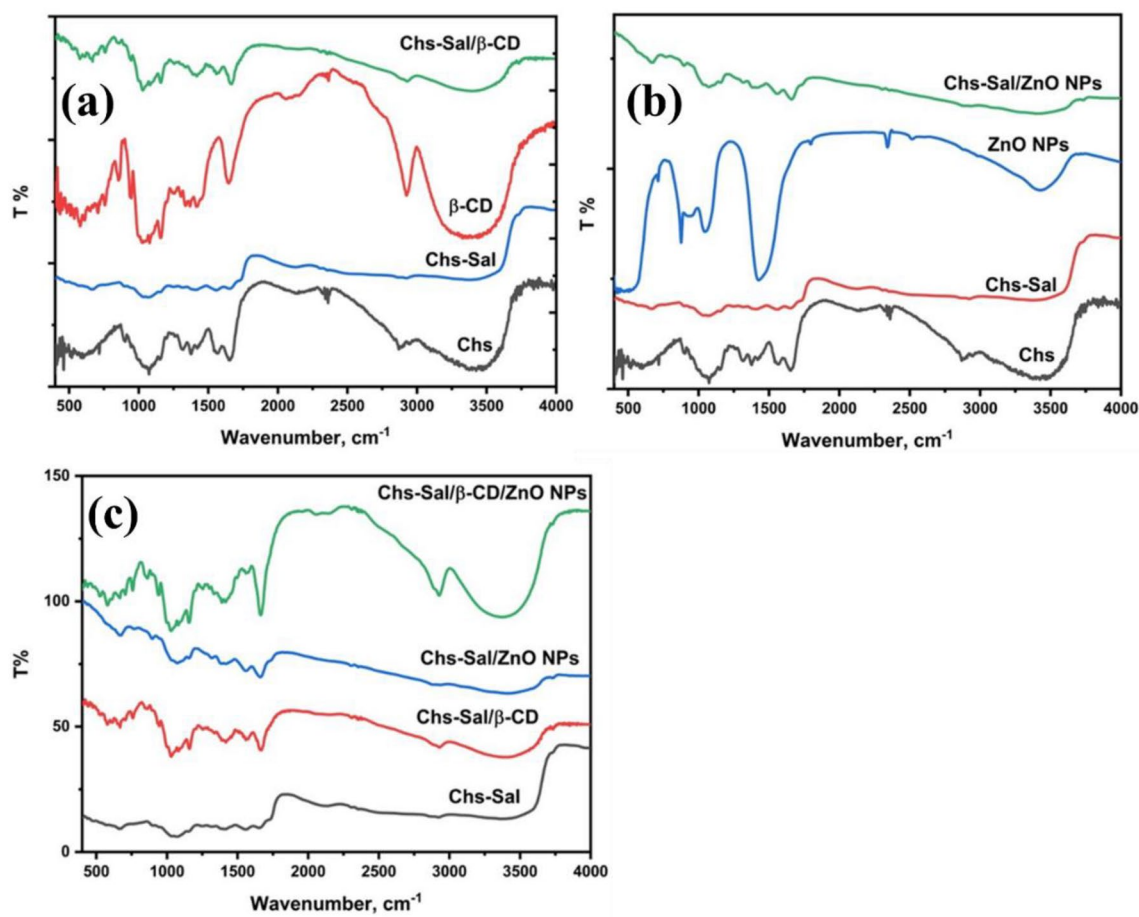
Figure 4. FT-IR spectra of (**a**) Chs, Chs-Sal, and β-CD and Chs-Sal/β-CD, (**b**) Chs, Chs-Sal, ZnO NPs and Chs, and Chs-Sal/ZnO NPs, and (**c**) Chs-Sal, Chs-Sal/β-CD, Chs-Sal/ZnO NPs and Chs-Sal/β-CD/ZnO NPs, respectively.

Functional groups	Wave number, cm^{-1}		
	Chs	Chs-Sal	$\Delta\nu$
ν[OH, NH] symmetric	3343	3373	-30
ν[CH aliphatic]	2978	2960	$+18$
ν[C–O]	1657	1649	$+8$
ν[C–N]	–	1631	–
ν[CH$_2$–OH]	1378	1370	$+7$
ν[C–O–C]	1068	1072	-4

Table 1. FT-IR changes of pure Chs and Chs-Sal polymer. $\nu = \nu$ (Chs-Sal polymer) $- \nu$(Chs).

Functional groups	Wave number, cm^{-1}				
	$\Delta\nu_1$	Chs-Sal polymer	Pseudopolyrotaxane	β-CD	$\Delta\nu_2$
ν[OH, NH] symmetric	$+23$	3373	3396	3389	$+7$
ν[CH aliphatic]	-60	2960	2900	2925	-25
ν[C–O]	$+19$	1649	1668	–	–
ν[CH$_2$–OH]	-22	1370	1158	1159	-1
ν[C–O–C]	-45	1072	1027	1028	-1

Table 2. FT-IR changes of β-CD, Chs-Sal polymer, and pseudopolyrotaxane polymer. $\Delta\nu_1 = \nu$(pseudopolyrotaxane) $- \nu$(Chs-Sal polymer), $\Delta\nu_2 = \nu$(pseudopolyrotaxane) $- \nu$(β-CD).

Functional groups	Wave number, cm^{-1}				
	Δv_1	Chs-Sal polymer	Chs-Sal/ZnO NPs	ZnO NPs	Δv_2
v[OH, NH] symmetric	+107	3373	3480	3333	+147
v[CH aliphatic]	−30	2960	2930	–	–
v[C–O]	−11	1649	1660	–	–
v[NH-bending]	+50	1570	1620	1553	+67
v[CH$_2$–OH]	+43	1370	1413	1393	+20
v[C–O–C]	+1	1072	1073	1090	−13

Table 3. FT-IR changes of Chs-Sal polymer, Chs-Sal/ZnO NPs composite and ZnO NPs. $\Delta v_1 = v$(Chs-Sal/ZnO NPs) − v(Chs-Sal polymer), $\Delta v_2 = v$(Chs-Sal/ZnO NPs) − v(ZnO NPs).

The absorption band of aliphatic C–H groups at 2927 cm^{-1}, was markedly shifted and increased in intensity. The absorption band at 1663 cm^{-1} was assigned to free C=O stretching vibration, and C–N group appeared at 1663 cm^{-1} with high intensity. The absorption bands at 1158 and 1028 cm^{-1} correspond to the stretching vibration of (CH$_2$–OH) group and C–O–C stretching became more intense and shifted to a lower wavenumber. The strong interaction between these functional groups in the polymer blend of pseudopolyrotaxane and ZnO NPs is indicated by these changes (shift and increase in intensity). The absorption band at 756 cm^{-1} appeared due to the stretching mode of the amide groups attached to ZnO NPs. Table 4 summarizes the differences between the absorption bands of the Chs-Sal/ZnO NPs polymer, Chs-Sal/β-CD polymer, and Chs-Sal/β-CD/ZnO NPs polymer.

Optical properties

UV–visible spectroscopy of Chs-Sal polymer, Chs-Sal/ZnO NPs composite, Chs-Sal/β-CD, and Chs-Sal/β-CD/ZnO NPs composite were recorded in the range of 200–800 nm at 25 °C (Fig. 5). The UV–visible spectrum of Chs-Sal polymer showed a broad peak at the region 327–360 nm due to the presence of π bond (–N=CH–). It's interesting to note that adding ZnO NPs and β-CD to the Chs-Sal polymer caused the characteristic peak to slightly shift blue, from 360 to 340 and 356 nm, respectively. Also, in the case of the addition of β-CD and

Functional groups	Wave number, cm^{-1}				
	Δv_1	Pseudopolyrotaxane	Chs-Sal/β-CD/ZnO NPs	Chs-Sal/ZnO NPs	Δv_2
v[OH, NH] symmetric	−21	3396	3375	3480	−105
v[CH aliphatic]	+27	2900	2927	2930	−3
v[C–O]	−5	1668	1663	1660	+3
v[CH$_2$–OH]	−2	1158	1156	1413	−257
v[C–O–C]	+1	1027	1028	1073	−45

Table 4. FT-IR changes of Chs-Sal/ZnO NPs polymer, Chs-Sal/β-CD polymer and Chs-Sal/β-CD/ZnO NPs polymer. $\Delta v_1 = v$(Chs-Sal/β-CD/ZnO NPs) − v(pseudopolyrotaxane), $\Delta v2 = v$(Chs-Sal/β-CD/ZnO NPs) − v(Chs-Sal/ZnO NPs).
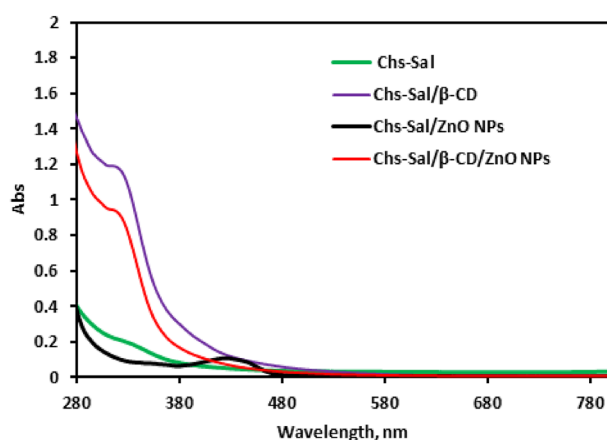

Figure 5. UV spectra of Chs-Sal, Chs-Sal/β-CD, Chs-Sal/ZnO NPs and Chs-Sal/β-CD/ZnO NPs.

ZnO NPs into Chs-Sal as a one pot-reaction gave a sharp peak in 439 nm. These data approved the formation of Chs-Sal/ZnO NPs, Chs-Sal/β-CD, and Chs-Sal/β-CD/ZnO NPs composite. Additionally, the energy gap Eg of the prepared polymers was calculated depending on the UV–visible absorption spectra according to Tauc's formula. The values of Eg for Chs-Sal, Chs-Sal/β-CD, Chs-Sal/ZnO NPs composite and Chs-Sal/β-CD/ZnO NPs composite were 4.4, 3.55, 2.65, and 3.11 eV, respectively. The lower Eg of Chs-Sal/β-CD/ZnO NPs composite (3.11 eV) compared to Chs-Sal (4.4 eV) makes the resistance of the sensor more likely to change in the presence of gas due to electron transition which leads to gas sensitivity improvement[37,60–63].

Thermal analysis

The thermal stability and heat resistance of the synthesized polymers were investigated using thermogravimetric analysis (TGA). TGA curves for Chs-Sal, Chs-Sal/ZnO NPs composite, Chs-Sal/β-CD, and Chs-Sal/β-CD/ZnO NPs composite are displayed in Fig. 6. Figure 6 clearly shows that, overall, the thermal stability of the Chs-Sal/β-CD composite was lower than that of the Chs-Sal polymer, while the weight loss at 350 °C was 40% and 34%, respectively. In the case of Chs-Sal was an organic polymer directly exposed to heat. But when the polymer was inserted into β-CD, it was preserved from the heat more and the loss of weight was less. The heat resistance of Chs-Sal/ZnO composite was improved by the incorporation of ZnO NPs because of the strong bond between zinc and oxygen in ZnO NPs, whereas the weight loss of Chs-Sal/ZnO at 350 °C was 17%. Conversely, when compared to Chs-Sal/β-CD, the thermal stability of the ZnO NPs composite increased by 55% at the same temperature. This was because the polymer's stability was increased by the addition of ZnO NPs. After addition of ZnO NPs into Chs-Sal/β-CD gave a more stable polymer, whereas the weight loss of Chs-Sal/β-CD/ZnO at 350 °C was 5%. The order of thermal stability for the four samples is based on the results shown in Fig. 6 and was as follow: Chs-Sal/β-CD/ZnO NPs ˃ Chs-Sal/ZnO NPs ˃ Chs-Sal/β-CD ˃ Chs-Sal.

Gas sensing properties

Figure 7b,c show the response of the polymer composite as a sensor towards various concentrations of NH_3 at RT. The Chs-Sal/β-CD/ZnO NPs composite sensor exhibited high sensing characteristics toward NH_3 down to 10 ppm concentration. It was observed that the sensor response was increased by increasing NH_3 concentration and recovered after purging the chamber with air, indicating reversible response characteristics of the composite (Fig. 7b). The sensor response and recovery times were 650 s and 350 s, respectively, indicating that Chs-Sal/β-CD/ZnO NPs composite is suitable for gas sensing applications. Besides, the selectivity of the Chs-Sal/β-CD/ZnO NPs composite sensor has also been studied at room temperature upon exposure to various 100 ppm gases/vapors (NH_3, chloroform, ethanol, and methanol) as depicted in Fig. 7e. The results indicate that the Chs-Sal/β-CD/ZnO NPs composite sensor exhibits the highest response when exposed to 100 ppm NH_3 which may to be due to its highest electron-donating ability compared to the other analytes[64]. Furthermore, the selective response of the composite toward NH_3 might be related to ZnO (transition metal oxide) which has more than one oxidation state and d^{10} electronic configuration that could retain cations with its filled orbital and be reduced when it reacted with reducing analyte like NH_3 to generate free electrons at RT[65]. Another reason for the high selectivity towards NH_3 may be due to the lone pair of electrons on the N atom, which are more likely to occupy the vacant orbital on Zn^{2+}, leading to the formation of a stronger binding energy[37], suggesting that the Chs-Sal/β-CD/ZnO NPs composite has excellent selectivity in NH_3-monitoring application. Figure 7a shows the response comparison of Chs-Sal, Chs-Sal/β-CD, Chs-Sal/ZnO NPs, and Chs-Sal/β-CD/ZnO NPs composite as sensors to 100 ppm of NH_3 at RT. The obtained observations indicated that Chs-Sal/β-CD/ZnO NPs composite exhibited improved NH_3 sensing response compared to other polymers (712 for Chs-Sal, and 6192 for Chs-Sal/β-CD/ZnO NPs, respectively). The limit of detection (LOD) is used as an important parameter for
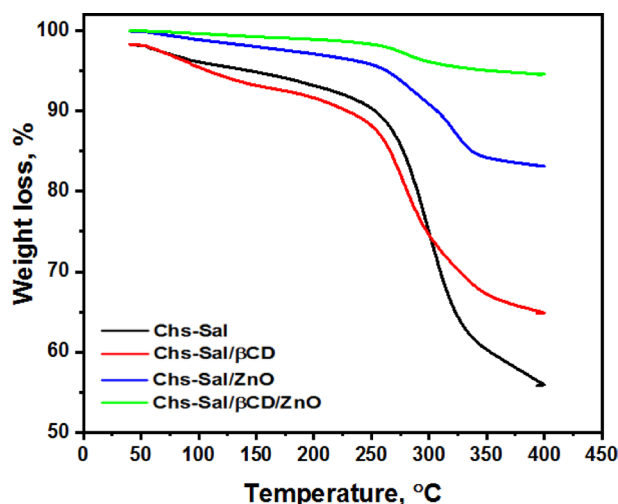

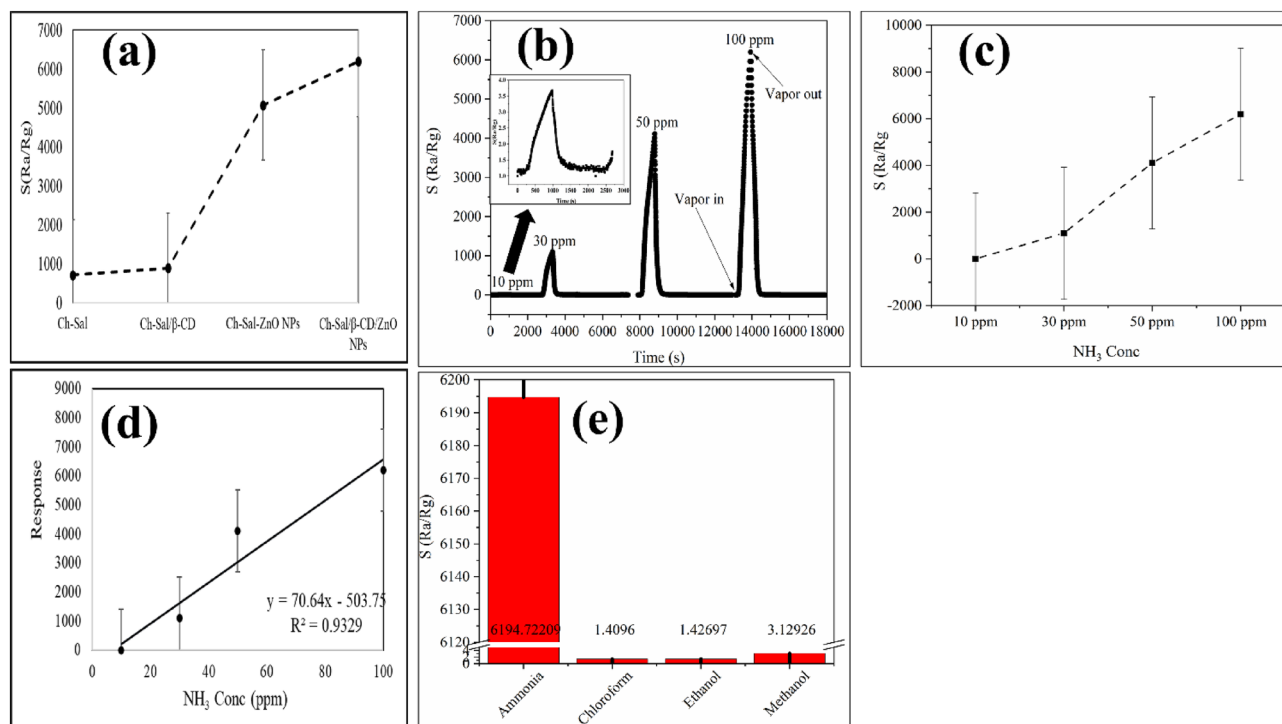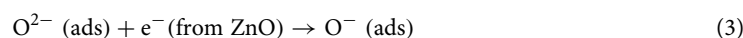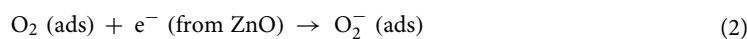**Figure 6.** TGA spectra of Chs-Sal, Chs-Sal/β-CD, Chs-Sal/ZnO NPs and Chs-Sal/β-CD/ZnO NPs.

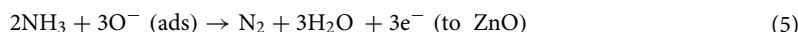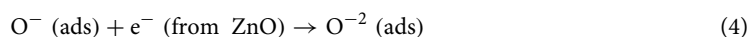**Figure 7.** Maximum response comparison of Chs-Sal, Chs-Sal/β-CD, Chs-Sal/ZnO NPs and Chs-Sal/β-CD/ZnO NPs towards NH$_3$ (100 ppm) at room temperature (**a**), gas responses of Chs-Sal/β-CD/ZnO NPs towards different concentrations of NH$_3$ (**b**), maximum response of Chs-Sal/β-CD/ZnO NPs vs different concentrations of NH$_3$ (**c**), linear fitting of Chs-Sal/β-CD/ZnO NPs response towards different NH$_3$ concentrations (**d**), and selective response of Chs-Sal/β-CD/ZnO NPs to some gases (100 ppm) at room temperature (**e**), respectively.

representing the sensing properties of the sensors, a high sensitivity usually has a low limit of detection. The calculations were achieved using the variation in the gas response at baseline (without analyte gas) using the root-mean-square deviation (rms). The rms deviation was calculated on 50 points at baseline[66] using RMS$_{noise}=\sqrt{\sum_i (Si - S)^2/N}$, where S$_i$ is the experimental data point, S is the corresponding value calculated from the curve-fitting, and N is the number of data points, respectively. The LOD is calculated as 3(RMS$_{noise}$/slope) (according to the IUPAC definition), where the slope is obtained from linear fitting of the response vs concentration (Fig. 7d). LOD of the prepared composite Chs-Sal/β-CD/ZnO NPs was 0.12 ppb surpassing the threshold value for NH$_3$ gas indicated by the National Institute for Occupational Safety and Health (NIOSH) (total weight average (TWA) permissible ammonia exposure limit is 25 ppm and the short-term exposure limit (ST) (for 15 min) is 35 ppm)[67]. Furthermore, this LOD is less than other NH$_3$ sensors such as 0.4 ppm[64], 11 ppm[68], and 0.78 ppb[69], respectively. The limit of quantification (LOQ) was calculated using 10(RMS$_{noise}$/slope)[70] and was 0.4 ppb which is lower than that reported in other studies[71–73].

Gas sensing behavior of the semiconductor is based on the strong interaction between the analyte gas molecules and the adsorbed oxygen species at the surface of the sensing material. Initially, the adsorbed oxygen molecules attract electrons from the ZnO NPs surface because they have high electron affinity[74], so, it is believed that the sensing mechanism occurs at the surface of the ZnO NPs. It was reported that defects such as Zn interstitials and oxygen vacancies that are found on ZnO NPs surface enable oxygen molecules in the ambient atmosphere to be adsorbed easily due to the differences in chemical potential energy[75]. When the Chs-Sal/β-CD/ZnO NPs composite is exposed to atmospheric air, the oxygen molecules trap the electrons from the conduction band of ZnO NPs and chemisorbed on the surface forming O^{2-}, O$^-$ and O^{2-} by increasing depletion layer width. This leads to increasing the surface resistance of the sensor. Upon injecting ammonia, the adsorbed oxygen species react with the NH$_3$ molecules forming H$_2$O, N$_2$, and three electrons which are injected into the conduction band of ZnO NPs by decreasing the depletion layer width and decreasing sensor resistance as a result. Upon the recovery of the sensor, the adsorbed ammonia molecules get desorbed from the ZnO NPs surface and increase the depletion layer width again and the resistance of the sensor is increased and returns to the initial baseline value[38]. The mechanism of the process is expressed by the following equations:

$$O_2 \text{ (gas)} \rightarrow O_2 \text{ (ads)} \tag{1}$$

$$O_2 \text{ (ads)} + e^- \text{ (from ZnO)} \rightarrow O_2^- \text{ (ads)} \tag{2}$$

$$O^{2-} \text{ (ads)} + e^- \text{ (from ZnO)} \rightarrow O^- \text{ (ads)} \tag{3}$$

$$O^- \ (ads) + e^- \ (from \ ZnO) \rightarrow O^{-2} \ (ads) \tag{4}$$

$$2NH_3 + 3O^- \ (ads) \rightarrow N_2 + 3H_2O \ + 3e^- \ (to \ ZnO) \tag{5}$$

In addition, The presence of OH groups of β-CD may also participate in the adsorption of NH_3 molecules through hydrogen bonding (hydrophilic outer side), and thus provides a favorable environment and more active sites for the adsorption of more NH_3 molecules[76–80]. Moreover, many vapor channels in the cavities of β-CD in addition to the inclusion of Ch-Sal-ZnO into these cavities may enhance the sensor response of Chs-Sal/β-CD/ZnO NPs composite[81]. Also, to further improve the sensitivity, it is necessary to introduce a conductive substrate such as ZnO NPs to increase the specific surface area of the composite[77]. Furthermore, the inner cavity of β-CD may occupied by traces of water vapor from the atmospheric air which may also interact with NH_3 vapor[82,83], leading to higher response value in the Chs-Sal/β-CD/ZnO NPs composite.

Conclusion

Stirring at room temperature of Chs polymer as an amine with Sal as a carbonyl component afforded Chs-Sal polymer. The obtained Chs-Sal was added to β-CD to form pseudopolyrotaxane inclusion complex and doped with ZnO NPs to produce the corresponding composite in a one-pot, adequate, simple, cost-effective, and eco-friendly environmentally method. Chs, Sal, ZnO NPs, and β-CD were reacted as one pot reaction to form Chs-Sal/β-CD/ZnO NPs composite polymer. These derivatives were confirmed by FT-IR and XRD analyses, while SEM analysis indicated remarkable morphological changes between them. UV–visible results confirmed the improvement of the optical properties of the prepared samples, as well as the decreasing of Eg of Chs-Sal/β-CD/ZnO NPs composite (3.11 eV) compared to Chs-Sal (4.4 eV) which enhances the sensitivity. The thermal stability of Chs-Sal polymer was enhanced by doping with ZnO NPs. Gas sensing results showed that the modification of chitosan-salicylaldehyde polymer through inclusion into β-CDs and doping with ZnO nanoparticles (NPs) showed high sensitivity (from 712 for Chs-Sal to 6192 for Chs-Sal/β-CD/ZnO NPs), good response and recovery times (650 s and 350 s, respectively) and low LOD and LOQ of 0.12 and 0.4 ppb, respectively, in addition to high selectivity towards NH_3 vapors which is related to its highest electron-donating ability compared to the other analytes, making them have a potential application prospect in NH_3 monitoring.

Data availability

All data generated or analyzed during this study are included in this published article.

References

1. Wang, W. *et al.* Chitosan derivatives and their application in biomedicine. *Int. J. Mol. Sci.* **21**, 487 (2020).
2. Spychalska, K., Zając, D., Baluta, S., Halicka, K. & Cabaj, J. Functional polymers structures for (bio)sensing application—A review. *Polymers* **12**, 1154 (2020).
3. Muhammad, A., Rahman, M. R., Baini, R. & Bin Bakri, M. K. 8—Applications of sustainable polymer composites in automobile and aerospace industry. In *Woodhead Publishing Series in Composites Science and Engineering* (ed. Rahman, M. R.) 185–207 (Woodhead Publishing, 2021).
4. Paolillo, S., Bose, R. K., Santana, M. H. & Grande, A. M. Intrinsic self-healing epoxies in polymer matrix composites (PMCs) for aerospace applications. *Polymers* **13**, 201 (2021).
5. Sadasivuni, K. K. *et al.* Chapter 11—Polymers in electronics. In *Polymer Science and Innovative Applications* (eds AlMaadeed, M. A. A. *et al.*) 365–392 (Elsevier, 2020).
6. Dorigato, A., Perin, D. & Pegoretti, A. Effect of the temperature and of the drawing conditions on the fracture behaviour of thermoplastic starch films for packaging applications. *J. Polym. Environ.* **28**, 3244–3255 (2020).
7. Kouhi, M., Prabhakaran, M. P. & Ramakrishna, S. Edible polymers: An insight into its application in food, biomedicine and cosmetics. *Trends Food Sci. Technol.* **103**, 248–263 (2020).
8. Guzik, M. W. *et al.* Robust process for high yield conversion of non-degradable polyethylene to a biodegradable plastic using a chemo-biotechnological approach. *Waste Manag.* **135**, 60–69 (2021).
9. Nasrollahzadeh, M., Shafiei, N., Nezafat, Z., Soheili Bidgoli, N. S. & Soleimani, F. Recent progresses in the application of cellulose, starch, alginate, gum, pectin, chitin and chitosan based (nano)catalysts in sustainable and selective oxidation reactions: A review. *Carbohydr. Polym.* **241**, 116353 (2020).
10. Song, Z., Li, G., Guan, F. & Liu, W. Application of chitin/chitosan and their derivatives in the papermaking industry. *Polymers* **10**, 389 (2018).
11. Jafari, Z., Rad, A. S., Baharfar, R., Asghari, S. & Esfahani, M. R. Synthesis and application of chitosan/tripolyphosphate/graphene oxide hydrogel as a new drug delivery system for sumatriptan succinate. *J. Mol. Liq.* **315**, 113835 (2020).
12. Rasines Mazo, A. *et al.* Ring opening polymerization of α-amino acids: Advances in synthesis, architecture and applications of polypeptides and their hybrids. *Chem. Soc. Rev.* **49**, 4737–4834 (2020).
13. Wegner, L. *et al.* Only carapace or the entire cephalothorax: Which is best to obtain chitosan from shrimp fishery waste?. *J. Mater. Cycles Waste Manag.* **23**, 1831–1837 (2021).
14. Ansari, K. R., Chauhan, D. S., Quraishi, M. A., Mazumder, M. A. J. & Singh, A. Chitosan Schiff base: An environmentally benign biological macromolecule as a new corrosion inhibitor for oil and gas industries. *Int. J. Biol. Macromol.* **144**, 305–315 (2020).
15. Radwan, M. F., Dardeer, H. M., Elboray, E. E. & Aly, M. F. Novel crystalline and thermally stable chitosan-chromone based polymers: Synthesis and characterization. *J. Mol. Struct.* **1241**, 130625 (2021).
16. Chauhan, D. S., Mazumder, M. A. J., Quraishi, M. A., Ansari, K. R. & Suleiman, R. K. Microwave-assisted synthesis of a new Piperonal-Chitosan Schiff base as a bio-inspired corrosion inhibitor for oil-well acidizing. *Int. J. Biol. Macromol.* **158**, 231–243 (2020).
17. Beyazit, N., Çakran, H. S., Cabir, A., Akışcan, Y. & Demetgül, C. Synthesis, characterization and antioxidant activity of chitosan Schiff base derivatives bearing (−)-gossypol. *Carbohydr. Polym.* **240**, 116333 (2020).

18. Sambasevam, K. P. *et al.* An optimization of fungal chitin grafted polyaniline for ammonia gas detection via Box Behnken design. *Int. J. Biol. Macromol.* **238**, 124079 (2023).
19. Mazlan, N. A., Sapari, J. M. & Sambasevam, K. P. Synthesis and fabrication of polyaniline/eggshell composite in ammonia detection. *J. Met. Mater. Miner.* **30**, 2 (2020).
20. Manimohan, M., Paulpandiyan, R., Pugalmani, S. & Sithique, M. A. Biologically active Co (II), Cu (II), Zn (II) centered water soluble novel isoniazid grafted O-carboxymethyl chitosan Schiff base ligand metal complexes: Synthesis, spectral characterisation and DNA nuclease activity. *Int. J. Biol. Macromol.* **163**, 801–816 (2020).
21. Parchegani, F., Amani, S. & Zendehdel, M. Eco-friendly chitosan Schiff base as an efficient sensor for trace anion detection. *Spectrochim. Acta Mol. Biomol. Spectrosc.* **255**, 119714 (2021).
22. Dragan, E. S. & Dinu, M. V. Advances in porous chitosan-based composite hydrogels: Synthesis and applications. *React. Funct. Polym.* **146**, 104372 (2020).
23. Takeshita, S., Zhao, S., Malfait, W. J. & Koebel, M. M. Chemistry of chitosan aerogels: Three-dimensional pore control for tailored applications. *Angew. Chem. Int. Ed.* **60**, 9828–9851 (2021).
24. Mittal, H. *et al.* Recent progress in the structural modification of chitosan for applications in diversified biomedical fields. *Eur. Polym. J.* **109**, 402–434 (2018).
25. Negm, N. A., Hefni, H. H. H., Abd-Elaal, A. A. A., Badr, E. A. & Abou Kana, M. T. H. Advancement on modification of chitosan biopolymer and its potential applications. *Int. J. Biol. Macromol.* **152**, 681–702 (2020).
26. Xiao, Z., Zhang, Y., Niu, Y., Ke, Q. & Kou, X. Cyclodextrins as carriers for volatile aroma compounds: A review. *Carbohydr. Polym.* **269**, 118292 (2021).
27. Jaafar, N. R. *et al.* Synergistic action of cyclodextrin glucanotransferase and maltogenic amylase improves the bioconversion of starch to malto-oligosaccharides. *Process Biochem.* **103**, 9–17 (2021).
28. Himat, A. S. *et al.* Starch-based novel ingredients for low glycemic food formulation. *Bioact. Carbohydr. Diet. Fibre* **26**, 100275 (2021).
29. Song, N. *et al.* Nanomaterials with supramolecular assembly based on AIE luminogens for theranostic applications. *Adv. Mater.* **32**, 2004208 (2020).
30. Velusamy, P. *et al.* Volatile organic compounds as potential biomarkers for noninvasive disease detection by nanosensors: A comprehensive review. *Crit. Rev. Anal. Chem.* https://doi.org/10.1080/10408347.2022.2043145 (2023).
31. Cheng, W.-Y., Chang, C.-R. & Fuh, H.-R. First principles study of NH_3, H_2S, Cl_2, and C_2H_2 gases adsorption on defective GaSe monolayer. *Appl. Surf. Sci.* **606**, 154722 (2022).
32. Liu, X., Zheng, W., Kumar, R., Kumar, M. & Zhang, J. Conducting polymer-based nanostructures for gas sensors. *Coord. Chem. Rev.* **462**, 214517 (2022).
33. Luo, K. *et al.* A sensitive and visual molecularly imprinted fluorescent sensor incorporating CaF_2 quantum dots and β-cyclodextrins for 5-hydroxymethylfurfural detection. *Anal. Chim. Acta* **1124**, 113–120 (2020).
34. Khattab, T. A., Dacrory, S., Abou-Yousef, H. & Kamel, S. Development of microporous cellulose-based smart xerogel reversible sensor via freeze drying for naked-eye detection of ammonia gas. *Carbohydr. Polym.* **210**, 196–203 (2019).
35. Karaduman, I., Er, E., Çelikkan, H., Erk, N. & Acar, S. Room-temperature ammonia gas sensor based on reduced graphene oxide nanocomposites decorated by Ag, Au and Pt nanoparticles. *J. Alloys Compd.* **722**, 569–578 (2017).
36. Dacrory, S., Saeed, A. M. & Abouzeid, R. E. A novel ammonia sensor based on cellulose/graphene oxide functionalized with ethylenediamine. *Express Polym. Lett.* **16**, 786–797 (2022).
37. Zhang, L., Zhang, H., Chen, C., Hu, Z. & Wang, J. Preparation and mechanism of high-performance ammonia sensor based on tungsten oxide and zinc oxide composite at room temperature. *Curr. Appl. Phys.* **45**, 30–36 (2023).
38. Al-darwesh, M. Y., Ibrahim, S. S., Faiad Naief, M., Mishaal Mohammed, A. & Chebbi, H. Synthesis and characterizations of zinc oxide nanoparticles and its ability to detect O_2 and NH_3 gases. *Results Chem.* **6**, 101064 (2023).
39. Han, K.-X., Wu, C.-C., Hsu, W.-F., Chien, W. & Yang, C.-F. Preparation of ultrafast ammonia sensor based on cross-linked ZnO nanorods coated with poly(3-hexylthiophene). *Synth. Met.* **299**, 117449 (2023).
40. Gao, R. *et al.* In-situ deposition of POMA/ZnO nanorods array film by vapor phase polymerization for detection of trace ammonia in human exhaled breath at room temperature. *Anal. Chim. Acta* **1199**, 339563 (2022).
41. Andre, R. S. *et al.* Hybrid layer-by-layer (LbL) films of polyaniline, graphene oxide and zinc oxide to detect ammonia. *Sensors Actuators B Chem.* **238**, 795–801 (2017).
42. Dardeer, H. M., Taha, A. G., Abouzeid, R. E. & Aly, M. F. Novel chitosan-acetyl isatin polymer derivatives: Synthesis, characterization, and applications in bone tissue engineering. *Biomass Convers. Biorefinery* https://doi.org/10.1007/s13399-022-03176-8 (2022).
43. Habib, I. Y. *et al.* Enhanced carbon monoxide-sensing properties of chromium-doped ZnO nanostructures. *Sci. Rep.* **9**, 9207 (2019).
44. Fahmy, A. *et al.* Nano-MnO_2/xanthan gum composite films for NO_2 gas sensing. *Mater. Chem. Phys.* **296**, 127277 (2023).
45. Dardeer, H. M. *et al.* Synthesis, application of a novel azo dye and its inclusion complex with beta-cyclodextrin onto polyester fabric. *Int. J. Text. Sci.* **6**, 79–87 (2017).
46. Dardeer, H. M. & Ebnalwaled, A. A. On improving the spectral response of organic dyes sensitizer based on β-cyclodextrin inclusion complex. *Optik (Stuttg)* **178**, 197–209 (2019).
47. Dardeer, H. M., Assran, A. S., Al-Hussain, S. A. & Toghan, A. Synthesis, spectroscopic and molecular docking studies of novel 10-heterylazo-9-anthrone derivatives as potential antimicrobial and anticancer agents. *J. Mol. Struct.* **1226**, 129359 (2021).
48. Michel, B. *et al.* Adsorption characterization of various modified β-cyclodextrins onto TEMPO-oxidized cellulose nanofibril membranes and cryogels. *Sustain. Chem. Pharm.* **24**, 100523 (2021).
49. Chen, W., Liu, D., Zhou, L., Li, Q. & Wu, D. Antioxidant activity of vitamin E enhanced by cyclodextrin inclusion complex. *Br. Food J.* **123**, 3988–3998 (2021).
50. Hossain, M. S., Hasan, M. M., Mahmud, M., Mobarak, M. B. & Ahmed, S. Assessment of crystallite size of UV-synthesized hydroxyapatite using different model equations. *Chem. Pap.* **77**, 463–471 (2023).
51. Gao, S. *et al.* Thiram/hydroxypropyl-β-cyclodextrin inclusion complex electrospun nanofibers for a fast dissolving water-based drug delivery system. *Colloids Surf. B Biointerfaces* **201**, 111625 (2021).
52. Liu, W. *et al.* Synthesis, characterization and antifungal efficacy of chitosan derivatives with triple quaternary ammonium groups. *Int. J. Biol. Macromol.* **114**, 942–949 (2018).
53. Barbosa, H. F. G., Attjioui, M., Ferreira, A. P. G., Moerschbacher, B. M. & Cavalheiro, É. T. G. New series of metal complexes by amphiphilic biopolymeric Schiff bases from modified chitosans: Preparation, characterization and effect of molecular weight on its biological applications. *Int. J. Biol. Macromol.* **145**, 417–428 (2020).
54. Huang, C. *et al.* Adsorption performance of chitosan Schiff base towards anionic dyes: Electrostatic interaction effects. *Chem. Phys. Lett.* **780**, 138958 (2021).
55. Guinesi, L. S. & Cavalheiro, É. T. G. Influence of some reactional parameters on the substitution degree of biopolymeric Schiff bases prepared from chitosan and salicylaldehyde. *Carbohydr. Polym.* **65**, 557–561 (2006).
56. Dardeer, H. M. & Toghan, A. A novel route for the synthesis of pseudopolyrotaxane containing γ-Cyclodextrin based on environmental waste recycling. *J. Mol. Struct.* **1227**, 129707 (2021).
57. Khowdiary, M. M., El-Henawy, A. A., Shawky, A. M., Sameeh, M. Y. & Negm, N. A. Synthesis, characterization and biocidal efficiency of quaternary ammonium polymers silver nanohybrids against sulfate reducing bacteria. *J. Mol. Liq.* **230**, 163–168 (2017).

58. Abdelrazek, E. M., Elashmawi, I. S., Hezma, A. M., Rajeh, A. & Kamal, M. Effect of an encapsulate carbon nanotubes (CNTs) on structural and electrical properties of PU/PVC nanocomposites. *Phys. B Condens. Matter* **502**, 48–55 (2016).
59. Esposito, P. *et al.* New treatment options for hyperkalemia in patients with chronic kidney disease. *J. Clin. Med.* **9**, 2337 (2020).
60. Kumar, R. R. *et al.* Ultrasensitive and light-activated NO_2 gas sensor based on networked MoS_2/ZnO nanohybrid with adsorption/desorption kinetics study. *Appl. Surf. Sci.* **536**, 147933 (2021).
61. Morales-Mendoza, J. E. & Paraguay-Delgado, F. Widening UV–Vis absorption band by Cu doped ZnO and ZnO/CuO composite. *Mater. Lett.* **291**, 129494 (2021).
62. Chaloeipote, G., Prathumwan, R., Subannajui, K., Wisitsoraat, A. & Wongchoosuk, C. 3D printed CuO semiconducting gas sensor for ammonia detection at room temperature. *Mater. Sci. Semicond. Process.* **123**, 105546 (2021).
63. Hu, Z., Zhang, H., Zhang, H., Yu, S. & Man, J. High performance NH_3 sensor based on CeO_2/In_2O_3 heterostructure for mutton preservation detection. *Mater. Sci. Semicond. Process.* **161**, 107475 (2023).
64. Ivanova, V. *et al.* Hybrid materials based on pyrene-substituted metallo phthalocyanines as sensing layers for ammonia detection: Effect of the number of pyrene substituents. *Sens. Actuators B Chem.* **375**, 132843 (2023).
65. Kwak, D., Lei, Y. & Maric, R. Ammonia gas sensors: A comprehensive review. *Talanta* **204**, 713–730 (2019).
66. Dua, V. *et al.* All-organic vapor sensor using inkjet-printed reduced graphene oxide. *Angew. Chem.* **122**, 2200–2203 (2010).
67. Barsan, M. E. *NIOSH Pocket Guide to Chemical Hazards* (DHHS Publication, 1997).
68. Mustapa, R., Mansor, Z. I. A. & Sambasevam, K. P. Fabrication of polyaniline based chemical sensor for ammonia gas detection. *J. Phys. Sci.* **29**, 9–16 (2018).
69. Yuan, Y. *et al.* Trace ppb-level NH_3 sensor based on single petal-like Ce-doped SnO_2. *Mater. Sci. Semicond. Process.* **157**, 107335 (2023).
70. Abdelkarem, K. *et al.* Efficient room temperature carbon dioxide gas sensor based on barium doped CuO thin films. *J. Mater. Sci.* **58**, 11568–11584 (2023).
71. Sambasevam, K. P. *et al.* Synthesis and application of polypyrrole/DBSA/boron nitride ternary composite as a potential chemical sensor for ammonia gas detection. *Orbital Electron. J. Chem.* **15**, 133–141 (2023).
72. Aflaha, R. *et al.* Improving ammonia sensing performance of quartz crystal microbalance (QCM) coated with nanofibers and polyaniline (PANi) overlay. *Biosens. Bioelectron. X* **13**, 100300 (2023).
73. Zakaria, S. A., Ahmadi, S. H. & Amini, M. H. Alginate/dye composite film-based colorimetric sensor for ammonia sensing: Chicken spoilage. *Food Control* **147**, 109575 (2023).
74. Bai, S. *et al.* Polythiophene-WO_3 hybrid architectures for low-temperature H_2S detection. *Sensors Actuators B Chem.* **197**, 142–148 (2014).
75. Kimiagar, S., Najafi, V., Witkowski, B., Pietruszka, R. & Godlewski, M. High performance and low temperature coal mine gas sensor activated by UV-irradiation. *Sci. Rep.* **8**, 16298 (2018).
76. Wu, S. S., Wei, M., Wei, W., Liu, Y. & Liu, S. Electrochemical aptasensor for aflatoxin B1 based on smart host-guest recognition of β-cyclodextrin polymer. *Biosens. Bioelectron.* **129**, 58–63 (2019).
77. Tu, X. *et al.* Mxene/carbon nanohorn/β-cyclodextrin-Metal-organic frameworks as high-performance electrochemical sensing platform for sensitive detection of carbendazim pesticide. *J. Hazard. Mater.* **396**, 122776 (2020).
78. Balu, S., Palanisamy, S., Velusamy, V., Yang, T. C. K. & El-Shafey, E.-S.I. Tin disulfide nanorod-graphene-β-cyclodextrin nanocomposites for sensing dopamine in rat brains and human blood serum. *Mater. Sci. Eng. C* **108**, 110367 (2020).
79. Iimura, Y., Fukuyama, M., Hibara, A., Harada, M. & Okada, T. Enhanced chiral recognition by β-cyclodextrin at liquid/liquid interfaces as revealed by chromatographic and interfacial tension measurements. *J. Colloid Interface Sci.* **508**, 469–475 (2017).
80. Wang, F. *et al.* Nanoliposome-encapsulated brinzolamide-hydropropyl-β-cyclodextrin inclusion complex: A potential therapeutic ocular drug-delivery system. *Front. Pharmacol.* **9**, 91 (2018).
81. Zhao, M.-X. *et al.* Synthesis, biocompatibility and cell labeling of l-arginine-functional β-cyclodextrin-modified quantum dot probes. *Biomaterials* **31**, 4401–4408 (2010).
82. Tao, Y. *et al.* Chiral recognition of d-tryptophan by confining high-energy water molecules inside the cavity of copper-modified β-cyclodextrin. *J. Phys. Chem. C* **119**, 8183–8190 (2015).
83. Liu, B. *et al.* Novel chitosan/ZnO bilayer film with enhanced humidity-tolerant property: Endowing triboelectric nanogenerator with acetone analysis capability. *Nano Energy* **78**, 105256 (2020).

Author contributions

The experiments were carried out by A.G.T. and A.M.S. The manuscript was written by all the authors. All authors discussed the results and commented on the manuscript according to thier speciality and experience.

Funding

Competing interests

The authors declare no competing interests.

Additional information

Correspondence and requests for materials should be addressed to A.M.S. or M.F.A.

Reprints and permissions information is available at www.nature.com/reprints.

Publisher's note Springer Nature remains neutral with regard to jurisdictional claims in published maps and institutional affiliations.